Architecture of the *Toxoplasma gondii* apical polar ring and its role in gliding motility and invasion

Ren, Bingjian; Haase, Romuald; Patray, Sharon; Nguyen, Quynh; Maco, Bohumil; Dos Santos Pacheco, Nicolas; Chang, Yi-Wei; Soldati-Favre, Dominique

How to cite

REN, Bingjian et al. Architecture of the *Toxoplasma gondii* apical polar ring and its role in gliding motility and invasion. In: Proceedings of the National Academy of Sciences of the United States of America, 2024, vol. 121, n° 46, p. e2416602121. doi: 10.1073/pnas.2416602121

This publication URL: https://archive-ouverte.unige.ch/unige:181361
Publication DOI: 10.1073/pnas.2416602121

PNAS RESEARCH ARTICLE | MICROBIOLOGY

Architecture of the *Toxoplasma gondii* apical polar ring and its role in gliding motility and invasion

Bingjian Ren[a,1], Romuald Haase[a,1], Sharon Patray[b,c], Quynh Nguyen[b,c], Bohumil Maco[a], Nicolas Dos Santos Pacheco[a,2], Yi-Wei Chang[b,c], and Dominique Soldati-Favre[a,3]

Affiliations are included on p. 11.

Edited by Margaret Phillips, The University of Texas Southwestern Medical Center, Dallas, TX; received August 16, 2024; accepted October 10, 2024

In *Toxoplasma gondii*, the conoid comprises a cone with spiraling tubulin fibers, preconoidal rings, and intraconoidal microtubules. This dynamic organelle undergoes extension and retraction through the apical polar ring (APR) during egress, gliding, and invasion. The forces involved in conoid extrusion are beginning to be understood, and its role in directing F-actin flux to the pellicular space, thereby controlling parasite motility, has been proposed. However, the contribution of the APR and its interactions with the conoid remain unclear. To gain insight into the APR architecture, ultrastructure expansion microscopy was applied to pinpoint known and newly identified APR proteins (APR2 to APR7). Our results revealed that the APR is constructed as a fixed multilayered structure. Notably, conditional depletion of APR2 resulted in significant impairments in motility and invasion. Electron microscopy and cryoelectron tomography revealed that depletion of APR2 alters APR integrity, affecting conoid extrusion and causing cytosolic leakage of F-actin. These findings implicate the APR structure in directing the apico-basal flux of F-actin to regulate parasite motility and invasion.

apicomplexa | *Toxoplasma gondii* | apical polar ring | motility | invasion

Significance

The obligate intracellular parasite *Toxoplasma gondii* relies on a dynamic organelle called the conoid, which traverses a multilayered apical polar ring (APR) during critical processes of gliding motility and host cell invasion. The conoid serves as an assembly platform for the actin–myosin machinery that drives parasite movement, while the lower APR layer organizes the parasite's cortical cytoskeleton, composed of subpellicular microtubules. Using advanced imaging techniques, such as cryoelectron tomography (cryo-ET), this study identified APR2 as a key structural component of the upper APR layer. This layer collaborates with the conoid to seal the compartment where F-actin is generated, thereby tightly controlling its flux. These findings provide deeper insights into the mechanisms that regulate parasite motility and invasion.

The phylum Apicomplexa encompasses parasites that pose a significant threat to the health of both animals and humans worldwide (1). Representative human pathogen species include *Plasmodium* spp., *Cryptosporidium* spp., and *Toxoplasma gondii*. A shared characteristic among apicomplexans is a structure located at the apical region of the parasites, known as the apical complex (2, 3). This complex comprises specialized secretory organelles, namely, rhoptries and micronemes, along with cytoskeletal structures. The apical complex serves as a central hub for multiple essential events, including the regulation of parasite motility, host cell egress, and invasion (4–8). Several layers of cytoskeletal elements confer structural rigidity to *T. gondii* including the alveolin network and inner membrane complex (IMC), composed of flattened membrane sacs, positioned directly below the plasma membrane (9–11). The 22 subpellicular microtubules (SPMTs) supporting the IMC (12) span two-thirds of the parasite's length. The apical polar ring (APR) (13) delineates the apical end of both the IMC and the SPMTs, presumably forming distinct structures (14). Additionally, the APR is thought to act as the microtubule organizing center (MTOC) during the initial stages of daughter parasite development (13, 15, 16). Anchored to the APR, the conoid is a dynamic organelle composed of a tubulin-based cone structure, capped by preconoidal rings (PCRs) and with two aligned intraconoidal microtubules (ICMTs) within. Aligned vesicles named MVs (microtubules-associated vesicles) have been observed along the ICMTs while an apical vesicle (AV) has been described above them, lying below the plasma membrane (17). Altogether, ICMTs, MVs, and AV facilitate iterative rhoptry discharge, crucial for parasite invasion and subversion of host cellular functions (7, 18). Conoid extrusion through the APR is powered by the myosin H (MyoH) positioned at the surface of the conoid (5, 19). The PCRs serve as a platform for the assembly of the gliding motility machinery, known as the glideosome, which includes the actin polymerizing protein Formin 1 (FRM1) (6, 9). Myosin A, found at the pellicular space between the IMC and the PM, then propels the complexes of adhesin and F-actin within the pellicle and toward the basal pole of the parasite, generating forward motion and resulting in F-actin accumulation at its base (5, 20). Although the contribution of the PCRs is now well established, the composition and role of the APR remain unclear. Depleting MyoH causes the F-actin to reroute inside the cytosol rather than within the pellicular space, which typically leads to its accumulation at the basal end of the parasite upon stimulation (5, 8). These findings suggest that conoid extrusion and the APR function as a "gatekeeper," steering F-actin in the pellicular space while preventing its unproductive entry into the cytosol. Additionally, during conoid extrusion, the conoid is securely tethered to the APR

Author contributions: B.R., R.H., Y.-W.C., and D.S.-F. designed research; B.R., R.H., S.P., Q.N., B.M., and N.D.S.P. performed research; B.R., R.H., S.P., Q.N., Y.-W.C., and D.S.-F. analyzed data; and B.R., R.H., Y.-W.C., and D.S.-F. wrote the paper.

The authors declare no competing interest.

This article is a PNAS Direct Submission.

[1]B.R. and R.H. contributed equally to this work.

[2]Present address: Department of Biochemistry, University of Cambridge, Cambridge CB2 1QW, United Kingdom.

[3]To whom correspondence may be addressed. Email: Dominique.soldati-favre@unige.ch.

This article contains supporting information online at https://www.pnas.org/lookup/suppl/doi:10.1073/pnas.2416602121/-/DCSupplemental.

Published November 8, 2024.

by RNG2, a protein spanning the space between the conoid base and the APR (21). The APR appears as a multilayered structure composed of several ring-shaped structures, including a ring of amorphous density [amorphous APR-associated density (AAD)] extending beyond the basal part of the ring and between the SPMTs (22, 23). Electron microscopy (EM) and cryoelectron tomography (cryo-ET) studies have shown that the APR is resistant to detergent treatment (22), and it remains unchanged during conoid extrusion/retraction. Knowledge about the APR's composition, assembly, and function is fractal. RNG1 is described as late marker of APR but is dispensable for parasite survival (24), whereas KinesinA (KinA) and APR1 function together to maintain the stability of the APR (13). Recent studies have identified additional APR proteins via proximity labeling in *T. gondii* (14) and *Plasmodium* spp (25). reporting a role in SPMTs anchorage.

Here, we used ultrastructure expansion microscopy (U-ExM) alongside conditional knockdown systems to determine the high-resolution localization of APR proteins and examine their roles in parasite survival. By colocalizing these proteins with RNG2, which marks the boundary between the conoid base and the apical end of the SPMTs, we categorized them into different structural layers. Detailed analysis of the APR2-depleted mutant by EM and cryo-ET showed morphological alteration of the APR, conoid positioning, and F-actin flux, leading to a significant defect in gliding motility. This finding supports the ability of the APR to tightly seal the pellicular compartment upon conoid extrusion to control motility and invasion.

Results

Repertoire of APR Proteins *in T. gondii*. During conoid extrusion, the position of the APR is fixed in *T. gondii* tachyzoites (Fig. 1*A*). To investigate the contribution of individual components of the APR structure, we applied the minimal auxin-inducible degron (mAID) system coupled with a HA epitope tag to localize and control the expression of the repertoire of APR proteins (26) (Table 1). This repertoire includes RNG1 (24), APR1 and Kinesin A (13), the recently described APR2 (27) as well as functionally uncharacterized proteins APR3 to APR7. Notably, APR2, APR3, APR4, APR6, and APR7 were previously localized by 3D structured illumination microscopy (3D-SIM) or U-ExM (14, 28, 29), while APR5, was identified independently using the ToxoDB website (30). The successful integration of mAID-HA at the endogenous loci was confirmed genomic PCR (*SI Appendix*, Fig. S1*A*), and localization at the apical tip was shown by Indirect immunofluorescence assay (IFA) (*SI Appendix*, Fig. S1*B*). Myosin E (MyoE) was previously reported to be at the apical tip based on endogenous C-terminal tagging (31). Using U-ExM, we confirmed the localization of all the selected proteins at the APR (Fig. 1*B*). Representative images of both extruded and retracted conoids revealed no significant alterations in the vertical localization of APR proteins during this process. Strikingly, U-ExM allowed us to precisely pinpoint those APR proteins in three distinct vertical layers namely, bottom, middle, and upper layer of the APR (Fig. 1 *A* and *B*). Proteins of the upper layer are distinctively observed above the SPMT level, while the proteins of the bottom layer seem to sit on top of them. APR3, APR4, and APR5 localized close to the conoid, whereas the other APR proteins were situated close to the SPMTs (Fig. 1*B*).

Next, we assessed the significance of APR2 to APR7 in the lytic cycle by confirming the depletion of these proteins through IFA (*SI Appendix*, Fig. S1*B*). Correct protein regulation as well as tagging of previously characterized APR proteins (APR1, KinA, and RNG1) was assessed by western blot analysis (Fig. 1*C* and *SI Appendix*, Fig. S1*C*). While depletion of APR3 and APR5 was achieved within 1 h of indole-3-aceticacid (IAA) treatment, depletion of APR4, APR6, and APR7 was incomplete even after 10 h of treatment (*SI Appendix*, Fig. S1*D*). Most of the APR proteins were fully depleted with prolonged auxin treatment (48 h), yet APR4 and APR7 did not fully disappear (Fig. 1*C* and *SI Appendix*, Fig. S1*D*). Hence, these genes were deleted by double homologous recombination to produce the *Δapr4* and *Δapr7* strains (*SI Appendix*, Fig. S1*E*). Plaque assays performed on the knockout and conditional depleted strains showed no significant reduction in plaque size except for APR2-mAID, which is required alone for an optimal lytic cycle of tachyzoites. (Fig. 1*D* and *SI Appendix*, Fig. S1*F*).

The APR is a Multilayer Structure. To assess the organization of APR proteins, we performed U-ExM imaging to examine their vertical position and diameter in more detail. Since RNG2 plays a crucial role in connecting the APR and conoid through its N- and C-terminal regions (21), RNG2 was used as marker to delineate the boundaries of the APR. All APR proteins were C-terminally Ty-tagged in Myc-RNG2-mAID-HA strain and proved to still be fitness conferring upon RNG2 depletion (*SI Appendix*, Fig. S2*A*). Western blot analysis confirmed the correct expression of all APR proteins in the Myc-RNG2-mAID-HA background migrating at expected sizes (*SI Appendix*, Fig. S2 *B* and *C*). Next, we examined both top-view and side-view images of the colocalization of RNG2-APR proteins via U-ExM (Fig. 2*A*) and analyzed their fluorescence profiles (*SI Appendix*, Fig. S3). Based on their vertical localization, we costained the APR proteins with either the N or C terminus of RNG2. APR5 was the only protein that overlapped with the N-terminal Myc tag of RNG2, indicating its presence in the "upper layer" of the APR (Fig. 2*A*). APR3 and APR4 were observed at a lower level than N-terminal-RNG2, localized to the "middle layer." APR2 partially colocalized with the C-terminal-RNG2. APR1, APR6, APR7, RNG1, and KinA, colocalized with the C-terminal-RNG2 at the bottom layer. Notably, APR7 exhibited a significantly larger diameter, and its signal extended beyond the APR layer both horizontally and vertically, reaching the space between the SPMTs (Fig. 2*A*). To further assess a possible association of APR proteins with the conoid, we utilized the properties of conoid detachment upon RNG2 depletion (32). All the APR proteins remained in place, whereas CPH1 (33), a conoid marker used as a control, was observed in the parasite's cytosol (Fig. 2*B*). High resolution localisation of APR proteins by U-ExM combined with detachment of the conoid upon RNG2 depletion provide evidence that APR proteins discriminate into a multilayer structure that are not associated with the conoid body.

APR2 Contributes to Efficient Gliding Motility and Invasion. APR2 stands out as the sole fitness-conferring protein among the functionally uncharacterized APR proteins described here. To dissect its function, we assessed various steps of the lytic cycle. Conditional knockdown of APR2 did not result in any defects in parasite replication (Fig. 3*A*). Additionally, induced egress stimulated by the inhibitor of phosphodiesterase, 5-Benzyl-3-isopropyl-1H-pyrazolo[4,3-d]pyrimidin-7(6H)-one (BIPPO) (34), was not affected (Fig. 3*B*). However, a clear defect in parasite dispersion upon egress, indicative of a motility issue, was observed (Fig. 3*C*). In parallel, depletion of APR2 did not impair microneme secretion, as measured by quantified secreted antigen in BIPPO-triggered parasites (Fig. 3*D*). Contrastingly, and confirming the observations made during the egress assay, the gliding motility of parasites lacking APR2 was compromised, as evidenced by the reduction of visible gliding trails under BIPPO induction compared to wild-type (WT) parasites (Fig. 3*E*). Given that conoid extrusion regulates parasite gliding ability, this process was assessed using U-ExM. In BIPPO-stimulated parasites lacking

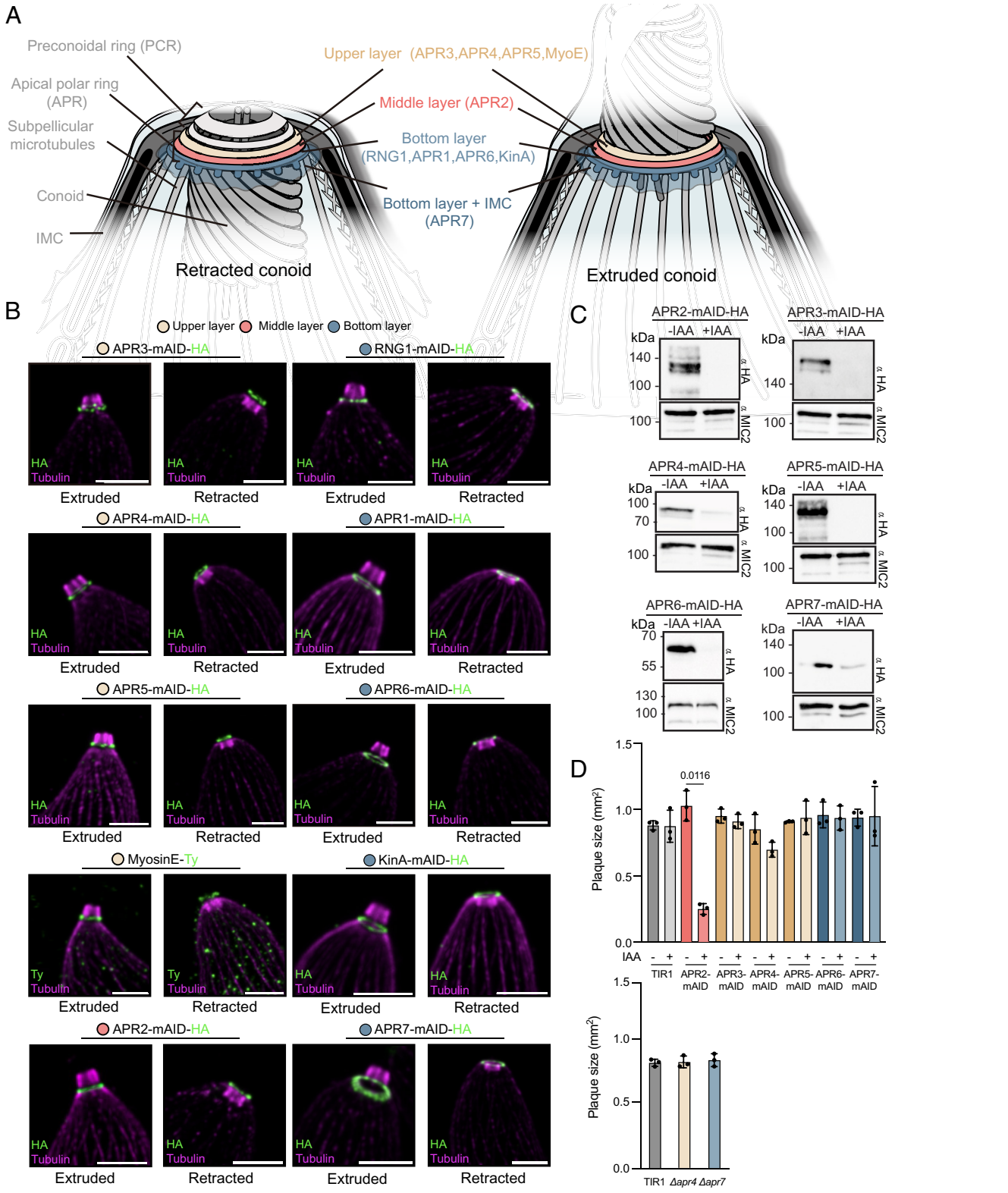

Fig. 1. Characterization of the localization and function of APR proteins. (*A*) Schematic of the APR of *T. gondii* in the conoid extruded state. (*B*) Localization of APR proteins via U-ExM in extracellular *T. gondii* parasites with extruded (*Left*) and retracted (*Right*) conoid. APR proteins are color-coded: upper layer (yellow), middle layer (red), and bottom layer (blue). (Scale bar, 3 μm.) (*C*) Protein depletion assessment of novel APR proteins by western blot in *T. gondii*. MIC2 served as a loading control. (*D*) Fitness of novel APR candidates by mAID conditional depletion or direct knockout: Quantification of plaque sizes obtained from three replicates to assess the fitness of novel APR candidates in *T. gondii* under mAID conditional depletion or direct knockout conditions. Statistical significance was determined via one-way ANOVA (*$P < 0.05$).

APR2, the conoid could be classified into three categories based on the vertical position: extruded, retracted, and partially extruded (conoid partially above the APR), the latter being significantly more observed in APR2-lacking parasites (Fig. 3*F*). Furthermore, approximately 10% of the APR2-depleted parasites were able to invade host cells compared to 50% in the absence of auxin and 60% in WT parasites (Fig. 3*G*). Host cell invasion critically depends on rhoptry discharge that can be quantified by counting

Table 1. List of the protein investigated in this study

Protein Name	Gene ID: ToxoDB	Gene ID: NCBI	Gene ID: UniProt	Localization: Experimental evidence	Localization: Method	Phenotype: Phenotype Score	Phenotype: Experimental evidence	Conservation: *Pf*	*Et*	*Nc*	*Sn*	*Cp*	Reference
RNG1	243545	EPR56572.1	S7UFG5_TOXGG	APR	3D-SIM	2.54	N/A	●	●	●	●	●	(14, 24)
RNG2	244470	EPR56603.1	S7VTU9_TOXGG	Conoid base and bottom APR	3D-SIM and U-ExM	−4.21	Strong Defect	●	●	●	●	●	(21, 32)
Myosin E	239560	EPR60465.1	S7URV6_TOXGG	Apical dot	Apical dot	0.11	No Defect	●	●	●	●	●	(31)
Kinesin A	267370	EPR57258.1	S7VW10_TOXGG	APR	3D-SIM	−2.7	Strong Defect	●	●	●	●	●	(13, 14)
APR1	315510	EPR58926.1	A0A125YVR1_TOXGG	APR	3D-SIM and immuno-EM	−0.05	Strong Defect	●	●	●	●	●	(13, 14)
APR2	227000	EPR62323.1	S7WD32_TOXGG	APR	3D-SIM and U-ExM	−3.2	N/A	●	●	●	●	●	(14, 26)
APR3	208340	EPR58029.1	S7VSI6_TOXGG	APR	3D-SIM	−0.81	N/A	●	●	●	●	●	(14)
APR4	219500	EPR63937.1	S7V275_TOXGG	APR	3D-SIM	0	N/A	●	●	●	●	●	(14)
APR5	299190	EPR59150.1	S7UN50_TOXGG	N/A	N/A	−2.6	N/A	●	●	●	●	●	This study
APR6	278780	EPR63159.1	S7W8B0_TOXGG	APR	3D-SIM	−2.8	N/A	●	●	●	●	●	(14)
APR7	320030	EPR58177.1	S7UK93_TOXGG	APR	3D-SIM	−0.19	N/A	●	●	●	●	●	(14)
										Fully conserved		●	
										Partially conserved		●	
										Not conserved		●	

This table describes the protein name as well as the accession number of the gene for ToxoDB (ME49 reference strain). The method of first identification by immunofluorescence, predicted fitness score, and experimental validation of the fitness score for each gene are listed. The conservation of each protein has been assessed by reverse blasting using the blast tool on EuPathDB.

the percentage of phosphorylated-STAT6 positive cells which reflects secretion of ROP16 (35, 36). No significant defect in rhoptry discharge was observed in the absence of APR2 as with glideosome associated connector (GAC) depleted parasites that are defective in motility, whereas aspartyl protease 3 (ASP3) depleted parasites failed to discharge the rhoptries (37), (Fig. 3*H*). Together, these data show that APR2 is selectively required for gliding motility and hence contributes to invasion.

APR2 Knockdown Destabilized the Middle Layer of the APR. Negative-stain transmission EM was used to examine the structural impact of APR2 depletion. In parasites with an extruded conoid, the structure of the APR is masked by the density of conoid and not easy to delineate (Fig. 4*A*). To obtain clearer images, we opted to detach the conoid from the apical pole without affecting the APR structure by depleting RNG2. The mAID-based simultaneous depletion of RNG2 and APR2 was confirmed by western blot analysis (*SI Appendix*, Fig. S4*A*). In the absence of APR2, the thickness of the APR region was considerably reduced, whereas the organization of SPMTs remained intact (Fig. 4*A* and *SI Appendix*, Fig. S4 *B* and *C*). This suggested that depletion of APR2 primarily leads to destabilization of the upper part of the APR, whereas the bottom layer, attached to the SPMTs, remains unaffected. Of relevance, APR3, APR4, and MyoE were Ty-tagged in APR2-mAiD and their localization under U-ExM and level of expression remained unchanged upon APR2 depletion (Fig. 4*B* and *SI Appendix*, Fig. S4*D*). In these strains, APR2 was still regulated and fitness conferring (*SI Appendix*, Fig. S4*E*).

Given the discrepancy between the APR markers remaining in place and the significant impact of APR2 depletion on the integrity of the upper layer of the APR, we examined the structure under more native conditions using cryo-ET (Fig. 4*C* and Movies S1 and S2). In WT parasites, we observed three distinguishable layers of APR, while depletion of APR2 caused destabilization of the middle layer (Fig. 4 *C* and *D* and Movies S1 and S2) reducing the width of the structure (Fig. 4*E*). By capturing images from the top view of the conoid structure, we measured the circumference of the APR and found it to be moderately increased upon APR2 depletion (Fig. 4 *F* and *G*). Such structural alterations in the upper layer of the APR might reduce the tightness of the APR around the extruded conoid, potentially explaining the observed defects in motility.

APR2 Depletion Alters Conoid Extrusion and Results in Abnormal F-Actin Flux. U-ExM revealed that in approximately 20% of stimulated parasites lacking APR2, the conoid was only partially extruded (Fig. 3*E*), while cryo-ET uncovered that it is the direction of conoid extrusion that is affected possibly due to the increased circumference of the APR (Fig. 5*A* and Movies S3 and S4). To validate this observation, we quantitatively measured the distance between the IMC collar and the PCRs on opposite sides of the conoid where such IMC–PCR distance difference is maximum in each cell (Fig. 5*B*). The results showed that APR2 depletion significantly increased the difference in IMC–PCR distance between both sides of the conoid cone, leading to a partially extruded and tilted conoid, a phenotype that we describe as "uneven extrusion." In our cryo-ET grids we observed that more than 55% of conoids extruded unevenly in APR2-depleted parasites, whereas this phenotype was observed in fewer than 15% of conoids in WT parasites (Fig. 5*C*). Conoid extrusion is dependent on efficient F-actin translocation and previous research suggested the existence of an F-actin connector localized at the apical region of the IMC (6), yet APR2 depletion did not destabilize this structure (*SI Appendix*, Fig. S4*F*). However, in over 40% of APR2-depleted parasites, F-actin was observed passing through the APR toward the parasite's cytosol (Fig. 5*D*, Dataset S2, and Movies S3 and S4). To gather more quantitative data, we expressed F-actin-recognizing chromobodies fused to green fluorescent proteins (CbGFP) in the APR2-mAID strain to track the F-actin flux, which, along with MyoA, powers gliding motility (5, 38). The expression of CbGFP was confirmed by western blot analysis and shown not to be affected by the conditional depletion of APR2 (*SI Appendix*, Fig. S4*G*). Moreover, the expression of CbGFP

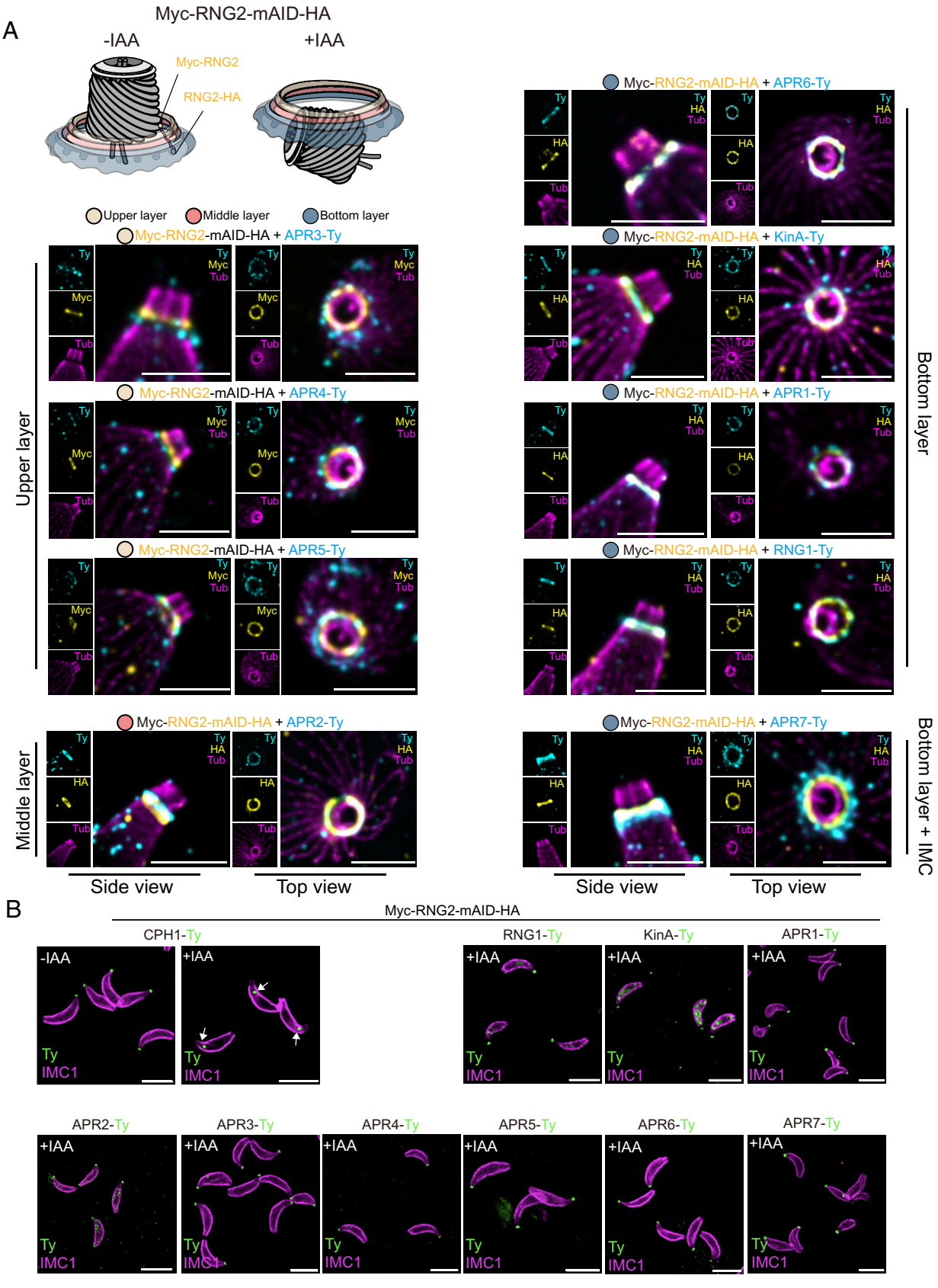

Fig. 2. Attribution of APR proteins in different layers by colocalization of RNG2. (*A*) Schematic of RNG2 localization on the APR of *T. gondii* in conoid extruded states and colocalization of APR proteins. Schematic representation illustrating RNG2 localization on the APR of *T. gondii* in conoid extruded states. The colocalization of APR proteins with Myc-tagged N termini (upper-layer APR proteins) or HA-tagged C termini (middle- and bottom-layer APR proteins) was visualized via U-ExM. Tub: tubulin; (Scale bar, 3 μm.) (*B*) Depletion of RNG2 does not affect the localization of APR proteins: Localization of APR proteins in *T. gondii* upon depletion of RNG2. The conoid marker CPH1 was used as the control. All selected APR proteins remained localized at the apical end in the absence of RNG2. (Scale bar, 3 μm.)

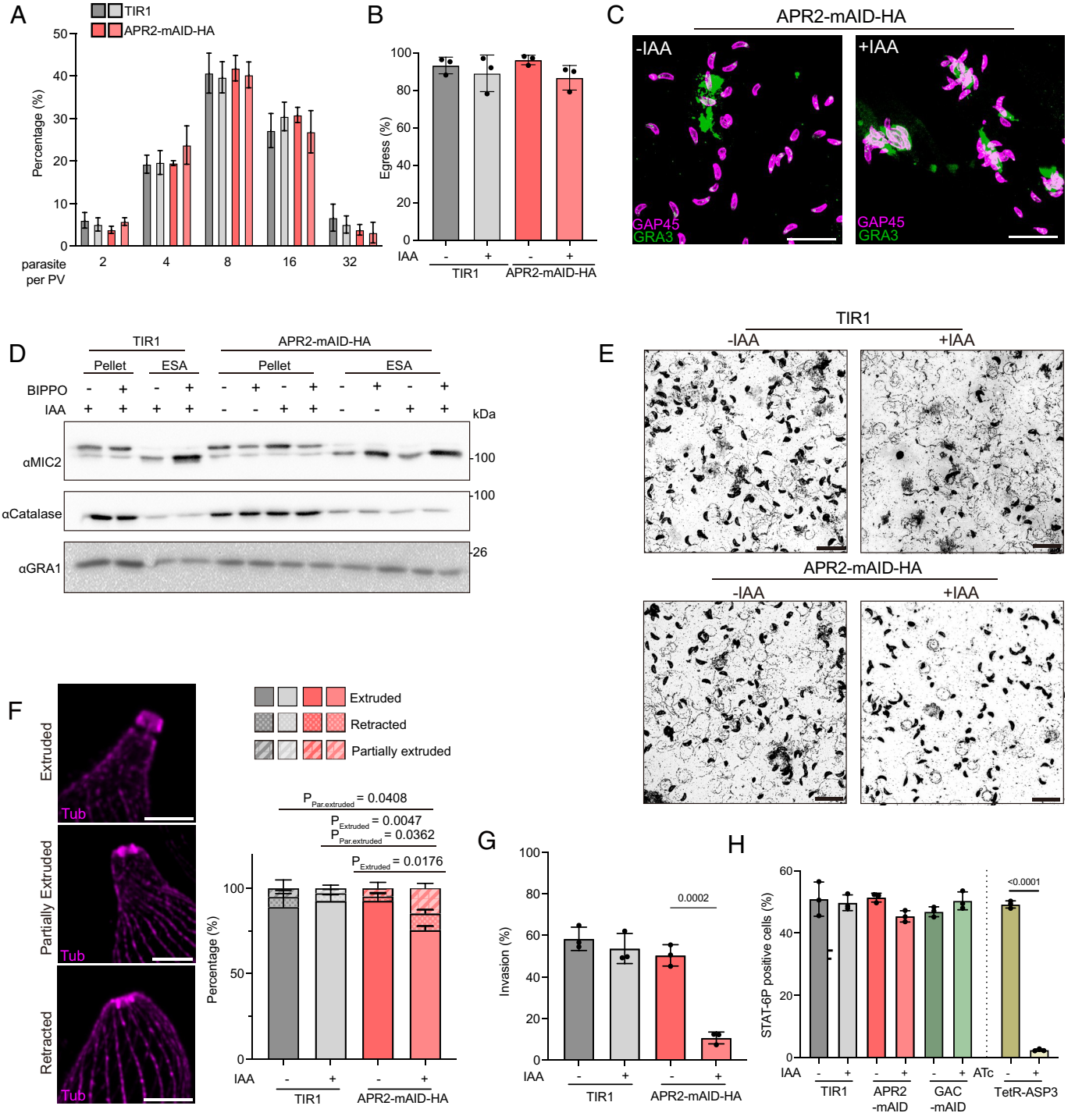

Fig. 3. Depletion of APR2 affects parasite gliding motility, invasion, and conoid extrusion. (*A*) APR2 does not contribute to parasite replication: Parasite replication was quantified by counting at least 100 parasitophorous vacuoles (PVs) in each replicate. Three replicates were conducted to generate the data. (*B*) Induced parasite egress is not affected in the absence of APR2: Parasites were cultured for 30 h before induction. The representative images showing parasite egress were presented in the *Right* panel. At least 100 PVs were quantified in each replicate. Three replicates were conducted to generate the data. (*C*) Representative images indicating the impaired dissemination after BIPPO-induced egress upon APR2-depletion. (Scale bar, 20 μm.) (*D*) Depletion of APR2 does not cause a defect in the induced microneme secretion assay: Unprocessed and processed MIC2s were detected in the parasite pellet or excreted secreted antigen (ESA) fraction. Catalase served as a control for the supernatant, and GRA1 was used as a loading control. (*E*) Gliding motility is impaired in APR2-depleted parasites: Gliding trails were visualized by staining with an SAG1 antibody. (Scale bar, 20 μm.) (*F*) APR2 contributes to conoid extrusion: Representative images of extruded, partially extruded, and retracted conoids are shown in the *Upper* panel, (Scale bar, 3 μm.) Tubulin (Tub) was used as a marker. Three replicates were conducted to generate the data. One-way ANOVA was used for statistical testing; *P* values are shown for $P < 0.05$. (*G*) APR2 depletion causes an invasion defect: Parasites were stained with SAG1 and GAP45 to visualize extracellular and total parasites. At least 200 parasites were used to quantify invasion events. Three replicates were conducted to generate the data. One-way ANOVA was used for statistical testing; *P* values are shown for $P < 0.05$. (*H*) Rhoptry discharge is not affected by depletion of APR2. The event was quantified by the percentage of cells with positive P-STAT6, which is indicative of parasite rhoptry discharge. At least 150 cells were quantified to plot the data. Conditional depletion of GAC and ASP3 served as controls for impaired gliding motility and rhoptry discharge. The data are presented from three independent replicates.

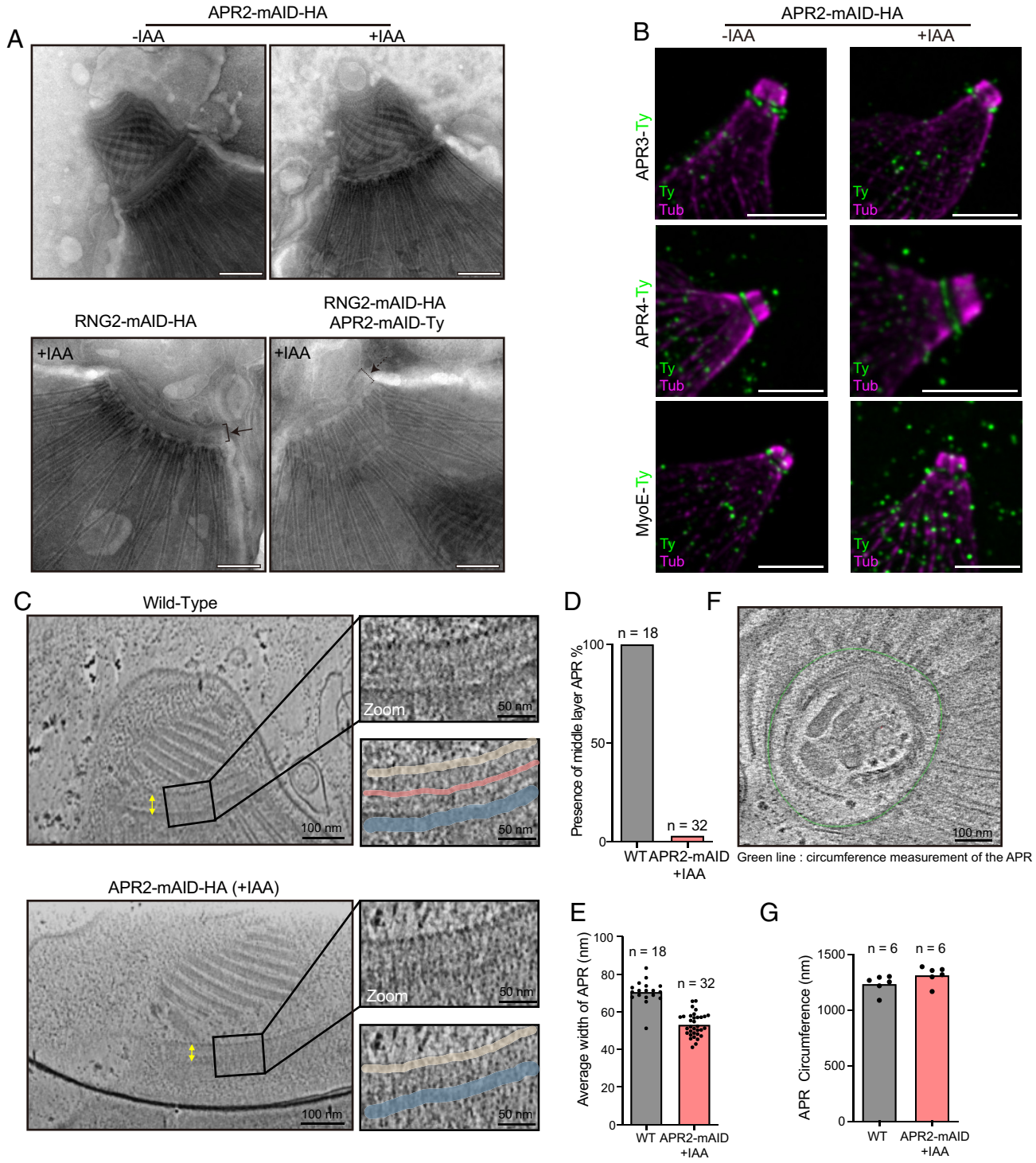

Fig. 4. APR2 contributes to the stability of the middle-layer APR. (*A*) Upper-layer APR is disrupted in the absence of APR2: Representative images showing destabilization of the upper-layer APR are presented; the thickness of upper APR is indicated by black arrow, (Scale bar, 200 nm.) (*B*) Depletion of APR2 does not cause mislocalization of upper-layer APR proteins. Representative images showing APR3, APR4, and MyoE as markers for the upper layer are presented. Tub: tubulin; (Scale bar, 3 μm.) (*C*) Cryo-ET tomograms of WT and APR2-depleted parasites showing a 2D plane where the APR is in view: An area of the APR is zoomed in (black box), and a zoomed-in view is shown on the *Right*. In the zoomed view, both the top and bottom layers of the APR can be observed in the WT and APR2-depleted parasites (colored yellow and blue). In the WT zoomed-in panel, a ring structure can be observed in the middle layer of the APR (colored in red). In the zoomed panel of APR2-depleted parasites, the ring structure in the middle layer was not observed. The width of the APR was measured from the top layer to the center of the bottom layer (yellow arrows). (*D*) Plot shows the percentage of WT and APR2-depleted parasites with a visible APR middle ring structure (WT: n = 16; APR2-mAID-HA +IAA: n = 33). (*E*) Plot showing the average APR width of WT and APR2-depleted parasites (WT: n = 18; APR2-mAID-HA +IAA: n = 32). (*F*) Representative tomogram showing the top view of an APR2-depleted parasite. A segmented outline of the APR (green circle) allows accurate measurement of the APR circumference in WT and APR2-depleted parasites. (*G*) Plot showing the average APR circumference of WT and APR2-depleted parasites (WT: n = 6 and APR2-mAID-HA +IAA: n = 6).

had minimal impact on parasite fitness as shown by plaque assay (*SI Appendix, Fig. S4H*). In non-auxin-treated gliding parasites, U-ExM revealed F-actin flux accumulating efficiently at the basal pole, as previously reported (39) (Fig. 5*E*). However, the absence of APR2 led to abnormal F-actin accumulation to the apical region, with some parasites still exhibiting basal accumulation (Fig. 5*E*).

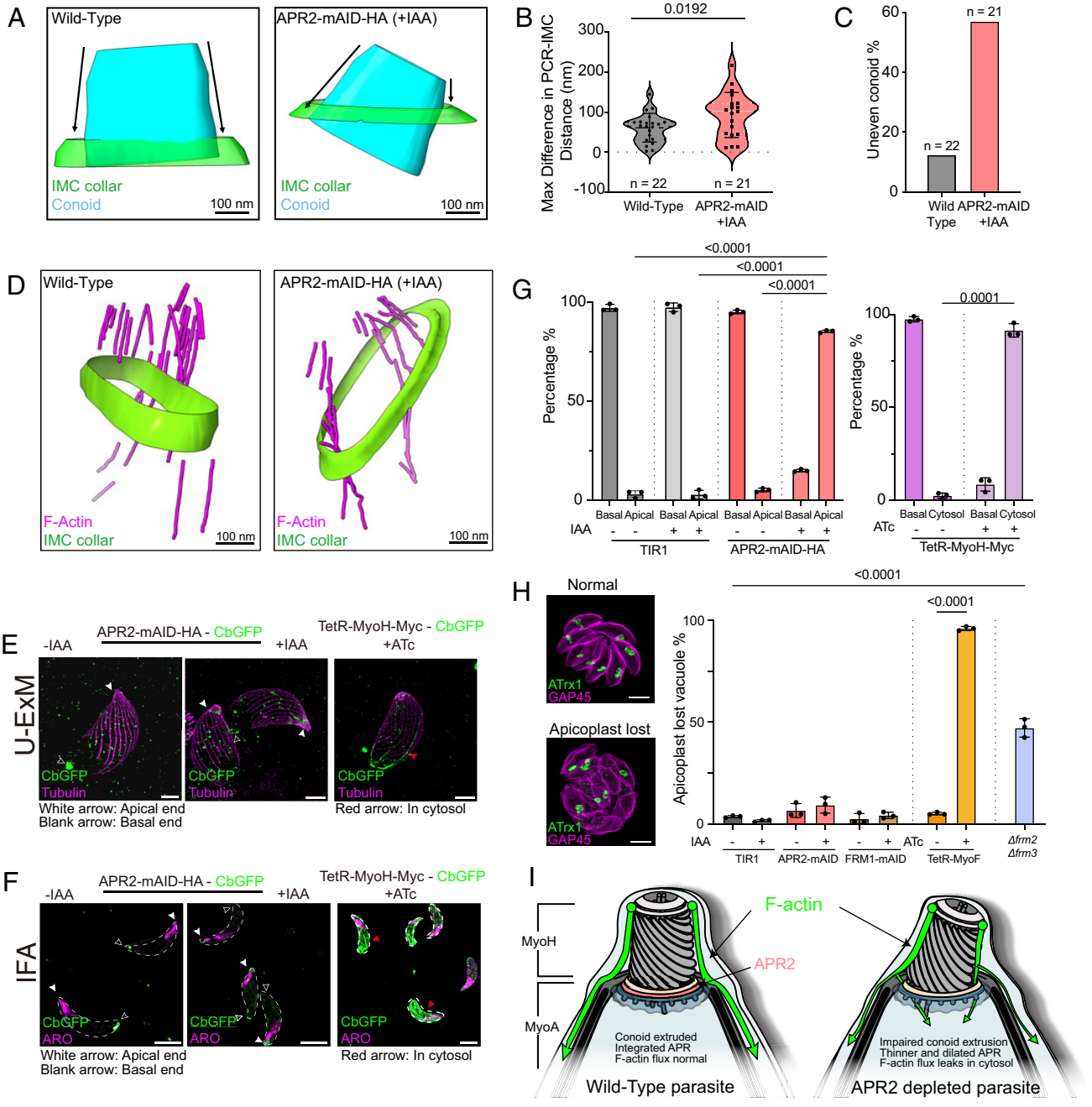

Fig. 5. APR2 is required for efficient F-actin translocation. (*A*) Segmentations of the IMC collar (green) and the conoid (blue) were generated from WT and APR2-depleted cryo-ET tomograms. The segmentation illustrates that the WT conoid extruded evenly, with a slight degree of conoid tilting tolerated. In contrast, APR2-depleted parasite segmentation revealed that the conoid extruded unevenly, with a relatively high degree of conoid tilting tolerated. The black arrows indicate the location and distance measured from the PCR to the upper layer of APR, which is located at the tip of the segmented IMC collar to assess the degree of uneven conoid extrusion. (*B*) Plot showing the measurement of the maximum difference in the distance from the PCR to the IMC in WT and APR2-depleted parasites from opposite sides of the conoid (WT: n = 22; APR2-mAID-HA +IAA: n = 21). (*C*) Plot showing the percentage of WT and APR2-depleted parasites with unevenly extruded conoids. Unevenly extruded conoids were designated those where the maximum difference in the PCR-IMC distance was greater than the WT mean (53.20) + SD (30.31) = 83.51 nm. (WT: n = 22, APR2-mAID-HA +IAA: n = 21). (*D*) Segmentations of F-actin (purple) and the IMC collar (green) were generated from cryo-ET tomograms of WT and APR2-depleted parasites. In the WT segmentations, F-actin flux was observed to channel outside the IMC into the pellicular space rather than leaking into the cytosolic space. In contrast, segmentations of APR2-depleted parasites show F-actin passing through the APR (APR is tightly associated with the segmented IMC collar on the cytosolic face with the upper APR layer coincides with the tip of the IMC collar). (*E*) Depletion of APR2 causes apical F-actin retention: Representative images showing F-actin apical accumulation are presented under U-ExM. (Scale bar, 3 μm.) (*F*) F-actin accumulation can be quantitatively assessed under classical IFA. (Scale bar, 3 μm.) ARO protein was used as an apical pole marker. (*G*) Quantification of apical F-actin retention in APR2-depleted parasites: Quantification was performed via an IFA in which the rhoptry surface protein ARO was used to mark the apical end. At least 100 parasites were counted in each replicate to generate the data. Three replicates were conducted. One-way ANOVA was used for statistical testing; *P* values are shown for $P < 0.05$. MyoH mutant was used as a cytosolic accumulation control. (*H*) Quantification of apicoplast loss events in APR2-depleted parasites. Parasites depleted in FRM1, FRM2/3 (39), and MyoF (42) were used as control. Quantification was performed via an IFA. Representative images for normal PV and apicoplast lost PV were presented. The apicoplast membrane protein ATrx1 (apicoplast Trx-like protein 1) was used to visualize the apicoplast for further quantification (43). (Scale bar, 3 μm.) At least 100 parasites were counted in each replicate to generate the data. Three replicates were conducted. (*I*) Scheme illustrating the effect of APR2 depletion. This scheme illustrates how APR2 depletion leads to impaired F-actin translocation, resulting in apical F-actin retention and uneven conoid extrusion in *T. gondii*.

This contrast with F-actin accumulation at the APR and apical IMC in the absence of MyoA (5, 40). Although APR2-depleted parasites accumulate F-actin in their cytosol, this phenotype is less severe compared to parasites expressing stably CbGFP and depleted for MyoH, which blocks conoid extrusion and leads to drastic cytosolic leakage of F-actin (Fig. 5 *E*–*G*). Given that APR2 depletion results in increased cytosolic F-actin, we investigated its potential impact on other F-actin-dependent processes, such as apicoplast inheritance, which relies on formin 2 protein (FRM2) (39, 41). Here, we compared parasites depleted of APR2 with those lacking both FRM2 and FRM3, as well as parasites depleted of FRM1 or myosin F (MyoF) which was identified as the critical motor for apicoplast segregation (39, 42).The results showed that while depletion of MyoF or FRM2/3 caused a significant increase in apicoplast loss, depletion of APR2 or FRM1 did not disrupt apicoplast segregation (Fig. 5*H*). Collectively, these results reveal that the depletion of APR2 alters the structure and circumference of the APR, which in turn impacts conoid extrusion. Although the parasites can produce F-actin and translocate from the apical region, the flux is altered due to a disruption in the gatekeeper mechanism that directs it to the pellicular space. This disruption results in a severe defect in motility and invasion without impacting the apicoplast inheritance (Fig. 5*I*).

Discussion

As a MTOC, the APR is conserved among all coccidian parasites. In *T. gondii* the APR has adopted a clearly defined thickness and distinguishable layers: the bottom part of the APR consists of a gear-like structure with repeating units, whereas the upper part appears as an irregular rubber band-like structure. Twenty-two microtubules are anchored to the bottom part of the APR, with attachment points located between the repeating structures at the bottom. The structure of the upper APR is less defined; different observation techniques seem to yield slightly different conclusions. EM images suggest that the upper APR is a continuous layer, whereas cryo-ET data indicate that the upper APR can be resolved into finer layers (22). The previously described APR1 and KinA are near the SPMTs, and their dual depletion destabilizes the APR (13). Considering that the bottom layer of the APR represents the nascent structure attached to the SPMTs, proteins located in this layer may play a role in APR biogenesis and stabilization. Additionally, high-resolution cryo-ET studies have revealed a ring of AAD, referred to as "AAD," located between the IMC and the tips of the SPMTs (22). The AAD appears to connect with the APR and extends into the spaces between adjacent SPMTs. Among the proteins investigated here, APR7 localizes to the bottom APR and exhibits a similar localization pattern extending from the bottom layer of the APR between the SPMT spaces. To further understand its implication in the APR structure, it will be interesting to examine APR7-depleted tachyzoites using cryo-ET. Although deletion of APR7 does not lead to growth defects, studies in *Plasmodium yoelii* have shown that genetic removal of the APR7 orthologue (*Py*APR2) in the ookinete stage results in impaired apical anchorage of the APR–SPMT complex and blocked parasite transmission in mosquitoes (25). Deeper investigation on *Py*APR2 identified several APR proteins (25), most of which do not have homologues in *T. gondii,* and only two homologues have been investigated (13, 44) (*SI Appendix*, Table S1). These findings suggest that although the APR is a conserved structure, its composition, assembly and roles may vary significantly among the Apicomplexa.

FRM1 is positioned at the PCRs and nucleates F-actin needed for conoid extrusion by MyoH (5). The latest cryo-ET analysis revealed that the filaments of actin are long enough to reach the pellicular space from the extruded conoid body (6). At the APR level, MyoA is responsible for the apico-basal flux of actin that generate motility (8). The presence of MyoE at the APR is intriguing; however, its depletion did not affect the parasite fitness, suggesting that this motor is not essential for F-actin flux and motility (31). U-ExM revealed the multilayer nature of the APR, allowing the classification of each APR proteins to one of its different layers. In contrast to RNG2 which tethers the APR to the conoid, all the APR proteins remain associated with the APR structure when the conoid is detached upon RNG2 depletion. Similarly to MyoE, the other APR proteins are dispensable and do not show apparent morphological defects by negative staining EM except for APR2. APR2 depleted parasites secrete their micronemes and can egress but failed to disseminate although conoid extrusion was only marginally affected based on U-ExM suggesting also that actin polymerization occurs normally. Taken together the results point to a restricted defect in gliding motility that results in impaired invasion. A recent study employing Cre-LoxP mediated gene depletion found that while depletion of APR2 leads to reduced invasion, no defects were observed in plaque assays (29).

The significant morphological alteration of the APR observed in the absence of APR2 through negative staining EM was at odds with the retained signal for APR3, APR4, and MyoE detected by U-ExM. This discrepancy suggests that experimental conditions for EM might have led to the detachment of the upper part of the APR structure. Consistent with this, a much more subtle morphological defect was observed using cryo-ET, which has been the panacea for investigating the apical ultrastructure of apicomplexans (6, 22, 23, 45–48). APR2 is localized in the middle region of the APR and is critical for the stability of a middle layer of the APR visible by cryo-ET and shown to disappear in the absence of APR2. Another notable impact of APR2 depletion observed by cryo-ET is the alteration in the APR circumference, likely affecting the positioning of the conoid during extrusion. In consequence, more actin filaments are visible in the cytosol and traversing the APR in this mutant. Actin filaments in *T. gondii* are generally shorter and less stable (49, 50). Under normal conditions, these filaments are also rapidly translocated by MyoA to the basal pole and are therefore not easily detectable in the pellicular space. To quantitatively investigate the fate of apically produced F-actin in stimulated extracellular parasites, we utilized stable expression of CbGFP in APR2-mAID and as a control in TetR-MyoH. In both mutants, F-actin is produced but leaks into the cytosol. While the complete block in conoid extrusion in the absence of MyoH prevents the apico-basal flux of F-actin, the phenotype observed upon APR2 deletion is intermediate, leading to a partial accumulation of F-actin at the basal pole These results align with the role of the upper layer of the APR as a barrier that, in conjunction with other structures involved in conoid extrusion, encloses the apical space and facilitates the proper transport of F-actin (5, 8). Since conoid extrusion depends on F-actin and MyoH which is anchored on the cone of the conoid, a F-actin connector localized at the apical region of the IMC is predicted to be crucial in order to transmit the force produced by the molecular motor (5). Despite its contribution to the F-actin flux, APR2 is unlikely serving as the connector since its depletion did not eliminate this structure seen in cryo-ET. Instead, APR2 likely plays a crucial role in maintaining the proper spatial organization of such F-actin connectors by preserving the proper configuration of the APR.

In conclusion, by combining genetic methods with various state-of-the-art microscopy techniques, we have gained a better understanding of the composition and role of the multilayered structure of the APR. APR2 accounts for an unreported layer of

the APR, and its absence leads to the loss of this structure, resulting in mispositioning of the conoid, which affects F-actin translocation and parasite gliding motility. These findings reveal a physiological function for the upper layer of the APR in sealing the space between the pellicle and the cytosol upon conoid extrusion. This work offers new mechanistic insights into the intricate connection between the dynamics conoid and the APR that serves as a gatekeeper for the flux of F-actin to quickly and tightly control motility in *T. gondii*.

Materials and Methods

Parasite Culture. *T. gondii* tachyzoites were cultured in human foreskin fibroblasts (HFFs) American Type Culture Collection in Dulbecco's modified Eagle's medium (DMEM, Gibco) supplemented with 5% fetal calf serum (Gibco), 2 mM glutamine, and 25 μg/mL gentamicin (Gibco). The transgenic lines were created via the RHΔKu80TIR1 strain (termed TIR1) to establish auxin-inducible knockdown and clean knockout lines. The knockdown lines generated via the Tet-inducible system were produced from the RHΔKu80 strain. For conditional knockdown, parasites were cultured in the presence of 500 μM IAA, referred to as +IAA, or 1 μg/mL anhydrotetracycline (ATc), referred to as +ATc. Unless otherwise specified, parasites were cultured for at least 24 h to allow protein degradation.

Generation of Transgenic Lines. Insertional tagging and gene depletion were achieved via the CRISPR-Cas9-mediated homology-directed repair system. The plasmid containing the sgRNA targeting the gene of interest was constructed on the basis of either the pSAG1::Cas9-U6::sgUPRT (51) or pU6-Universal (52) background. The HDR template was amplified via KOD polymerase (Merck), with specific primers and plasmid templates detailed in Dataset S1. *T. gondii* was transfected via electroporation (53). Each transfection utilized 40 μg of plasmid and 100 μL of PCR products. To generate the lines stably expressing CbGFP, the pTub-CbGFP cassette was amplified from pTub-CbGFP-Ty-HX (primers in Dataset S1), digested by EcoRI + AvrII, and ligated into the vector pUPRT-pTub-G13-Ty. 60 μg plasmid was linearized by Kpn I for the transfection. Parasites carrying an HXGPRT cassette were selected using 25 mg/mL mycophenolic acid and 50 mg/mL xanthine. Parasites carrying a Dihydrofolate reductase cassette were selected via the use of 1 μM pyrimethamine. Parasites with Uracil phosphoribosyltransferase (UPRT) locus replaced by CbGFP expressing cassette were selected via the use of 5 μM 5-Fluoro-2′-deoxyuridine (FUDR). For the generation of APR2-mAID-HA strains, two clones have been generated independently.

IFA. HFFs were seeded on coverslips, infected with *T. gondii* tachyzoites, and incubated at 37 °C for 15 to 24 h. Parasites were fixed with either 4% PFA/0.05% glutaraldehyde (PFA-GA) in PBS or ice-cold methanol, neutralized in 0.1 M glycine-PBS for 3 to 5 min in the case of PFA-GA fixation, and blocked in PBS containing 2% bovine serum albumine (BSA). The antibodies were incubated for 1 h in PBS/2% BSA, and the samples were washed with PBS between the primary and secondary antibody incubations. Coverslips were mounted with DAPI Fluoromount-G (Southern Biotech). Images were acquired via a Zeiss (LSM700) or Leica scanning confocal microscope (Leica Stellaris 5) with a 63×/1.4 oil objective. Image processing for publication was performed via ImageJ software. Details regarding the antibody dilutions are summarized in Dataset S1.

Plaque Assay. HFF monolayers were infected with freshly egressed parasites and incubated for 7 d at 37 °C. The cells were fixed with 4% paraformaldehyde and 0.005% glutaraldehyde (PFA-GA), followed by neutralization in 0.1 M glycine/PBS. After being washed with PBS, the cells were stained with crystal violet. To measure the plaque area, images of the monolayers were analyzed via ImageJ software.

Intracellular Replication Assay. HFF cells seeded on coverslips were infected with freshly egressed parasites and incubated at 37 °C for 24 h. The cells were then collected and fixed with 4% paraformaldehyde and 0.05% glutaraldehyde (PFA-GA) in PBS, followed by neutralization with 0.1 M glycine/PBS. Immunofluorescence labeling using antibodies against GAP45 was performed to visualize the vacuoles.

Egress Assay. Coverslips with HFF monolayers were infected with *T. gondii* tachyzoites and incubated at 37 °C for 30 h to allow growth. The cells were subsequently treated with DMEM containing BIPPO or DMSO for 10 min at 37 °C. Following treatment, the coverslips were fixed with PFA-GA and processed for immunofluorescence labeling as described previously via antibodies against GAP45 and GRA3.

Invasion Assay. HFF monolayers were infected with *T. gondii* tachyzoites, centrifuged at 1,000 × g for 1 min, and then incubated at 37 °C for 30 min to allow invasion. The cells were fixed with PFA-GA, blocked with 2% PBS-BSA for 20 min, and incubated with anti-SAG1 antibodies for 1 h. After being washed three times with PBS, the cells and antibodies were fixed with 1% formaldehyde for 7 min and permeabilized with 0.2% Triton X-100 in PBS for 20 min. Subsequently, the cells were incubated with anti-GAP45 antibodies, washed three times, and incubated with the appropriate secondary antibodies.

Microneme Secretion Assay. Freshly egressed parasites were washed twice in warm DMEM. The samples were subsequently pelleted and resuspended in media containing BIPPO or DMSO, followed by incubation at 37 °C for 10 min. The pellets and the supernatant [excretedsecreted antigen (ESA)] were separated via centrifugation at 2,000 × g. The ESA fraction was further purified via centrifugation at 5,000 × g to remove cellular debris. The pellet fractions were washed once with PBS to eliminate residual ESA. Both pellets and ESAs were analyzed by western blotting using antibodies against MIC2, catalase, and GRA1. The assay was repeated three times, and a representative replicate is presented in the manuscript. Images were captured via ImageLab software (Bio-Rad).

Phospho-STAT6 Rhoptry Discharge Assay. Freshly egressed parasites (5×10^4) pretreated for 48 h with IAA or ATc were used to infect HFF monolayer-coated coverslips. The cells were subjected to brief centrifugation (1,000 × g for 1 min) and then incubated at 37 °C for 18 h. After fixation with cold methanol (7 min at −20 °C), blocking was performed with 5% bovine serum albumin in PBS. Immunodetection was carried out with an anti-phospho-STAT6 antibody (Cell Signaling).

Gliding Trail Assay. The protocol for the gliding trail assay was adapted from a published method (54). Freshly egressed parasites pretreated with or without IAA were washed once with PBS and resuspended in a calcium saline solution. A drop of the sample was then placed onto poly-L-lysine-coated coverslips, and the parasites were allowed to glide at 37 °C for 15 min before fixation with 4% paraformaldehyde/0.05% glutaraldehyde in PBS for 7 min. Gliding trails were visualized via IFAs with α-SAG1 antibody hybridoma. The calcium saline solution comprised 0.5 mL of 2× 2-[4-(2-hydroxyethyl)piperazin-1-yl]ethanesulfonic acid (HEPES) buffer, 50 μL of 100 mM $CaCl_2$ (5 mM), and 450 μL of sterile water. The 2× HEPES buffer contained NaCl (274 mM), KCl (10 mM), Na_2HPO4 (2 mM), glucose (11 mM), and HEPES (42 mM) and was adjusted to pH 7.05.

F-Actin Basal Accumulation Assay. Freshly induced parasites pretreated with IAA or ATc were washed once with warm DMEM, resuspended in PBS containing BIPPO, and then seeded on poly-D-lysine-coated coverslips. The coverslips were incubated at 37 °C for 10 min and fixed with 4% paraformaldehyde and 0.05% glutaraldehyde (PFA-GA) in PBS, followed by neutralization with 0.1 M glycine/PBS. Subsequently, the fixed coverslips were subjected to immunolabeling with anti-GFP and anti-ARO antibodies for quantification. Representative images were captured via a Leica scanning confocal microscope (Leica Stellaris 5) with a 63×/1.4 oil objective. Image processing for publication was conducted via ImageJ software.

Apicoplast Lost Assay. HFF cells were seeded on coverslips and subsequently infected with freshly egressed parasites. Infected cells were incubated at 37 °C for 30 h. After incubation, cells were fixed with 4% paraformaldehyde and 0.05% glutaraldehyde (PFA-GA) in PBS, followed by neutralization with 0.1 M glycine/PBS. Immunofluorescence labeling was then performed using antibodies against GAP45 and ATrx1 (43) to visualize the vacuoles and apicoplast, respectively.

Data, Materials, and Software Availability. All study data are included in the article and/or supporting information.

ACKNOWLEDGMENTS. We thank for their technical assistance and imaging analysis, the team at the Bioimaging Core Facility, François Prodon,

Olivier Brun, and Nicolas Liaudet. We thank Gloria Lin for the use of GAC-mAID-HA strain as a control in our experiments. The project is funded by the Swiss NSF to D.S.-F. (310030_215445 and CRSII5_198545). David and Lucile Packard Fellowship for Science and Engineering (2019-69645) and a Burroughs Wellcome Fund Investigators in the Pathogenesis of Infectious Disease Program award (1022785) to Y.-W.C. B.R. is funded by European Molecular Biology Organization Postdoctoral Fellowship (ALTF 531-2021). We thank the Perelman School of Medicine EM Resource Lab Core Facility (RRID:SCR_022375), the Beckman Center for Cryo-EM (CrossRef: 10.13039/100000997), and the Singh Center for Nanotechnology at the University of Pennsylvania for hosting and supporting the use of the cryo-ET facilities.

Author affiliations: [a]Department of Microbiology and Molecular Medicine, Faculty of Medicine, University of Geneva, Geneva 1206, Switzerland; [b]Department of Biochemistry and Biophysics, Perelman School of Medicine, University of Pennsylvania, Philadelphia, PA 19104; and [c]Institute of Structural Biology, Perelman School of Medicine, University of Pennsylvania, Philadelphia, PA 19104

1. S. M. Adl *et al.*, Diversity, nomenclature, and taxonomy of protists. *Syst. Biol.* **56**, 684–689 (2007).
2. N. Dos Santos Pacheco, N. Tosetti, L. Koreny, R. F. Waller, D. Soldati-Favre, Evolution, composition, assembly, and function of the conoid in apicomplexa. *Trends Parasitol.* **36**, 688–704 (2020).
3. B. Anderson-White *et al.*, Cytoskeleton assembly in Toxoplasma gondii cell division. *Int. Rev. Cell Mol. Biol.* **298**, 1–31 (2012).
4. D. J. Dubois, D. Soldati-Favre, Biogenesis and secretion of micronemes in Toxoplasma gondii. *Cell Microbiol.* **21**, e13018 (2019).
5. N. Dos Santos Pacheco *et al.*, Conoid extrusion regulates glideosome assembly to control motility and invasion in Apicomplexa. *Nat. Microbiol.* **7**, 1777–1790 (2022).
6. M. Martinez *et al.*, Origin and arrangement of actin filaments for gliding motility in apicomplexan parasites revealed by cryo-electron tomography. *Nat. Commun.* **14**, 4800 (2023).
7. N. Dos Santos Pacheco *et al.*, Sustained rhoptry docking and discharge requires Toxoplasma gondii intraconoidal microtubule-associated proteins. *Nat. Commun.* **15**, 379 (2024).
8. R. Haase, N. Dos Santos Pacheco, D. Soldati-Favre, Nanoscale imaging of the conoid and functional dissection of its dynamics in Apicomplexa. *Curr. Opin. Microbiol.* **70**, 102226 (2022).
9. N. Tosetti *et al.*, Essential function of the alveolin network in the subpellicular microtubules and conoid assembly in Toxoplasma gondii. *Elife* **9**, e56635 (2020).
10. A. L. Chen *et al.*, Novel insights into the composition and function of the Toxoplasma IMC sutures. *Cell. Microbiol.* **19**, e12678 (2017).
11. C. R. Harding, M. Meissner, The inner membrane complex through development of Toxoplasma gondii and plasmodium. *Cell. Microbiol.* **16**, 632–641 (2014).
12. N. S. Morrissette, L. D. Sibley, Cytoskeleton of apicomplexan parasites. *Microbiol. Mol. Biol. Rev.* **66**, 21–38 (2002).
13. J. M. Leung *et al.*, Stability and function of a putative microtubule-organizing center in the human parasite Toxoplasma gondii. *Mol. Biol. Cell* **28**, 1361–1378 (2017).
14. L. Koreny *et al.*, Molecular characterization of the conoid complex in Toxoplasma reveals its conservation in all apicomplexans, including Plasmodium species. *PLoS Biol.* **19**, e3001081 (2021).
15. B. A. Nichols, M. L. Chiappino, Cytoskeleton of Toxoplasma gondii. *J. Protozool.* **34**, 217–226 (1987).
16. R. Haase, A. Puthenpurackal, B. Maco, A. Guérin, D. Soldati-Favre, γ-tubulin complex controls the nucleation of tubulin-based structures in Apicomplexa. *Mol. Biol. Cell* **35**, ar121 (2024).
17. S. K. Mageswaran *et al.*, In situ ultrastructures of two evolutionarily distant apicomplexan rhoptry secretion systems. *Nat. Commun.* **12**, 4983 (2021).
18. A. T. Heaslip, S. C. Ems-McClung, K. Hu, TgICMAP1 is a novel microtubule binding protein in Toxoplasma gondii. *PLoS One* **4**, e7406 (2009).
19. A. Graindorge *et al.*, The conoid associated motor MyoH is indispensable for Toxoplasma gondii entry and exit from host cells. *PLoS Pathog.* **12**, e1005388 (2016).
20. M. Meissner, D. Schlüter, D. Soldati, Role of Toxoplasma gondii myosin A in powering parasite gliding and host cell invasion. *Science* **298**, 837–840 (2002).
21. N. J. Katris *et al.*, The apical complex provides a regulated gateway for secretion of invasion factors in Toxoplasma. *PLoS Pathog.* **10**, e1004074 (2014).
22. L. Gui *et al.*, Cryo-tomography reveals rigid-body motion and organization of apicomplexan invasion machinery. *Nat. Commun.* **14**, 1775 (2023).
23. Z. Li *et al.*, Cryo-electron tomography of Toxoplasma gondii indicates that the conoid fiber may be derived from microtubules. *Adv. Sci.* **10**, 2206595 (2023).
24. J. Q. Tran *et al.*, RNG1 is a late marker of the apical polar ring in Toxoplasma gondii. *Cytoskeleton (Hoboken)* **67**, 586–598 (2010).
25. P. Qian *et al.*, Apical anchorage and stabilization of subpellicular microtubules by apical polar ring ensures Plasmodium ookinete infection in mosquito. *Nat. Commun.* **13**, 7465 (2022).
26. K. M. Brown, S. Long, L. D. Sibley, Conditional knockdown of proteins using auxin-inducible degron (AID) fusions in Toxoplasma gondii. *Bio-Protocol* **8**, e2728 (2018).
27. L. F. Arias Padilla, J. M. Lopez, A. Shibata, J. M. Murray, K. Hu, The initiation and early development of apical-basal polarity in Toxoplasma gondii. *J. Cell Sci.* **137**, jcs263436 (2024), 10.1242/jcs.263436.
28. N. Dos Santos Pacheco, D. Soldati-Favre, "Coupling auxin-inducible degron system with ultrastructure expansion microscopy to accelerate the discovery of gene function in Toxoplasma gondii" in *Parasite Genomics: Methods and Protocols*, L. M. de Pablos, J. Sotillo, Eds. (Springer US, New York, NY, 2021), pp. 121–137, 10.1007/978-1-0716-1681-9_8.
29. L. F. A. Padilla, J. M. Murray, K. Hu, The initiation and early development of the tubulin-containing cytoskeleton in the human parasite Toxoplasma gondii. *Mol. Biol. Cell* **35**, ar37 (2024).
30. O. S. Harb, D. S. Roos, "ToxoDB: Functional genomics resource for toxoplasma and related organisms" in *Toxoplasma gondii: Methods and Protocols*, C. J. Tonkin, Ed. (Springer, US, New York, NY, 2020), pp. 27–47, 10.1007/978-1-4939-9857-9_2.
31. K. Frénal *et al.*, Myosin-dependent cell-cell communication controls synchronicity of division in acute and chronic stages of Toxoplasma gondii. *Nat. Commun.* **8**, 15710 (2017).
32. R. Haase *et al.*, RNG2 tethers the conoid to the apical polar ring in *Toxoplasma gondii*: A key mechanism in parasite motility and invasion. bioRxiv [Preprint] (2024). https://doi.org/10.1101/2024.08.29.610260 (Accessed 1 September 2024).
33. S. Long, B. Anthony, L. L. Drewry, L. D. Sibley, A conserved ankyrin repeat-containing protein regulates conoid stability, motility and cell invasion in Toxoplasma gondii. *Nat. Commun.* **8**, 2236 (2017).
34. B. L. Howard *et al.*, Identification of potent phosphodiesterase inhibitors that demonstrate cyclic nucleotide-dependent functions in apicomplexan parasites. *ACS Chem. Biol.* **10**, 1145–1154 (2015).
35. Y.-C. Ong, M. L. Reese, J. C. Boothroyd, Toxoplasma rhoptry protein 16 (ROP16) subverts host function by direct tyrosine phosphorylation of STAT6*. *J. Biol. Chem.* **285**, 28731–28740 (2010).
36. J. P. J. Saeij *et al.*, Toxoplasma co-opts host gene expression by injection of a polymorphic kinase homologue. *Nature* **445**, 324–327 (2007).
37. S. K. Dogga *et al.*, A druggable secretory protein maturase of Toxoplasma essential for invasion and egress. *Elife* **6**, e27480 (2017).
38. J. Periz *et al.*, Toxoplasma gondii F-actin forms an extensive filamentous network required for material exchange and parasite maturation. *Elife* **6**, e24119 (2017).
39. N. Tosetti, N. Dos Santos Pacheco, D. Soldati-Favre, D. Jacot, Three F-actin assembly centers regulate organelle inheritance, cell-cell communication and motility in Toxoplasma gondii. *Elife* **8**, e42669 (2019).
40. M. Del Rosario *et al.*, Apicomplexan F-actin is required for efficient nuclear entry during host cell invasion. *EMBO Rep.* **20**, e48896 (2019).
41. J. F. Stortz *et al.*, Formin-2 drives polymerisation of actin filaments enabling segregation of apicoplasts and cytokinesis in Plasmodium falciparum. *Elife* **8**, e49030 (2019).
42. D. Jacot, W. Daher, D. Soldati-Favre, Toxoplasma gondii myosin F, an essential motor for centrosomes positioning and apicoplast inheritance. *EMBO J.* **32**, 1702–1716 (2013).
43. A. E. DeRocher *et al.*, A thioredoxin family protein of the apicoplast periphery identifies abundant candidate transport vesicles in Toxoplasma gondii. *Eukaryot. Cell* **7**, 1518–1529 (2008).
44. G. Lentini *et al.*, Identification and characterization of Toxoplasma SIP, a conserved apicomplexan cytoskeleton protein involved in maintaining the shape, motility and virulence of the parasite. *Cell Microbiol.* **17**, 62–78 (2015).
45. M. Martinez *et al.*, Rhoptry secretion system structure and priming in Plasmodium falciparum revealed using in situ cryo-electron tomography. *Nat. Microbiol.* **7**, 1230–1238 (2022).
46. L. M. Theveny *et al.*, Parasitology meets cryo-electron tomography–Exciting prospects await. *Trends Parasitol.* **38**, 365–378 (2022).
47. L.-A. Segev-Zarko *et al.*, Cryo-electron tomography with mixed-scale dense neural networks reveals key steps in deployment of Toxoplasma invasion machinery. *PNAS Nexus* **1**, pgac183 (2022).
48. Y. Sun Stella *et al.*, Cryogenic electron tomography reveals novel structures in the apical complex of Plasmodium falciparum. *mBio* **15**, e0286423 (2024).
49. N. Sahoo, W. Beatty, J. Heuser, D. Sept, L. D. Sibley, Unusual kinetic and structural properties control rapid assembly and turnover of actin in the parasite Toxoplasma gondii. *Mol. Biol. Cell* **17**, 895–906 (2006).
50. K. L. Hvorecny, T. E. Sladewski, E. M. De La Cruz, J. M. Kollman, A. T. Heaslip, Toxoplasma gondii actin filaments are tuned for rapid disassembly and turnover. *Nat. Commun.* **15**, 1840 (2024).
51. B. Shen, M. Brown Kevin, D. Lee Tobie, L. D. Sibley, Efficient gene disruption in diverse strains of Toxoplasma gondii using CRISPR/CAS9. *mBio* **5**, e01114-14 (2014), 10.1128/mbio.01114-01114.
52. S. M. Sidik, C. G. Hackett, F. Tran, N. J. Westwood, S. Lourido, Efficient genome engineering of Toxoplasma gondii using CRISPR/Cas9. *PLoS One* **9**, e100450 (2014).
53. D. Soldati, J. C. Boothroyd, Transient transfection and expression in the obligate intracellular parasite Toxoplasma gondii. *Science* **260**, 349–352 (1993).
54. C. Roumégous *et al.*, Identification of new components of the basal pole of Toxoplasma gondii provides novel insights into its molecular organization and functions. *Front. Cell. Infect. Microbiol.* **12**, 1010038 (2022).